Propagation of X-Ray Wavefield Beams in a Slightly Deformed Crystal

U. Bonse and W. Graeff

Institut für Physik, University of Dortmund, Dortmund-Hombruch, Germany

(Z. Naturforsch. **28 a**, 558–564 [1973]; received 30 January 1973)

Dedicated to Prof. G. Borrmann on the occasion of his 65th birthday

Bragg case wavefield beams are generated with MoKα radiation in a uniformly bent silicon crystal. The propagation of the wavefield beams is investigated by measuring their exit locations and intensities. Very good agreement is found with locations and intensities calculated from the Bragg case beam propagation theory formulated by one of the authors [1a] some time ago. Both low and high absorption wavefields were investigated.

1. Introduction

Over the last three decades dynamical X-ray diffraction by perfect crystals has been investigated by many authors both theoretically and experimentally. At least for the case of only two strong waves in the crystal, the mechanism of dynamical X-ray diffraction is fairly well understood by now. Experimental results in general agree closely with the theory as originally developed by EWALD [1], VON LAUE [2], and others.

In the *imperfect* crystal X-ray diffraction can be very complicated and so are most of the theories treating the general case of the deformed crystal. However in the *slightly deformed* crystal very interesting and at the same time with comparatively simple theories interpretable effects are observed.

In a slightly deformed lattice the two plane wave components still stay together as in the perfect crystal and set up a dynamical wavefield. However, the direction of its energy flow, which can be detected as the direction of the so called wavefield beam, remains no longer constant [3a] as in the perfect lattice. In the slightly deformed crystal a wavefield beam may sharply bend with radii of curvature as small as 10 microns [3]. Connected with the bending of the beam is a shift of energy from one plane wave component to the other. At the same time the degree of absorption usually changes, i. e. initially weakly absorbed wavefields may become normally absorbed and vice versa. Due to the effect of bending of wavefield beams the reflection power of crystals can be changed drastically [4–6]. Also, the deviation of wavefield beams with the help of deformed crystals may possibly be used in a new kind of X-ray diffraction optics for the purpose of constructing focussing or imaging devices for X-rays. It is found worth while therefore to study the diffraction of X-rays by slightly deformed crystals in greater detail.

As was already pointed out the general treatment of X-ray diffraction by an imperfect lattice is very complicated. Fortunately, in the case of sufficiently small deformation, simple beam propagation theories [1a, 7–9] so far appear to account fairly well for the observations. It is the purpose of this paper to report experimental results on wavefields excited in the Bragg case and propagating in uniformly bent silicon crystals. Beam paths and intensities are calculated from the theory formulated by one of the authors some time ago [1a]. The agreement with the observations is very good. Most of the beam tracing experiments so far have been performed in the Laue case where the simpler theory of PENNING and POLDER [7] can be applied.

Reprint requests to Prof. Dr. U. Bonse, Lehrstuhl für Exp. Physik I der Universität Dortmund, *D-4600 Dortmund-Hombruch*, Postfach 500.

2. Experiments

The experimental set up is illustrated in Figure 1. The primary molybdenum Kα X-ray beam is collimated by asymmetric 444 reflection from a silicon crystal reducing the horizontal divergence to about 0.17 sec of arc. With the help of slit 1 and slit 2 a ribbon like beam of about 80 microns width is shaped which is incident on the silicon sample crystal and diffracted by it in symmetrical 444 reflection. At the entrance surface of the sample the surface reflected beam R_0 and a Bragg type wavefield beam entering the crystal are excited. Under the influence of the sample's deformation the wavefield beam is deviated and may eventually curve back to the surface where part of the beam exits as beam R_1. The rest of it is directed back into the the crystal by Bragg case partial internal reflection.

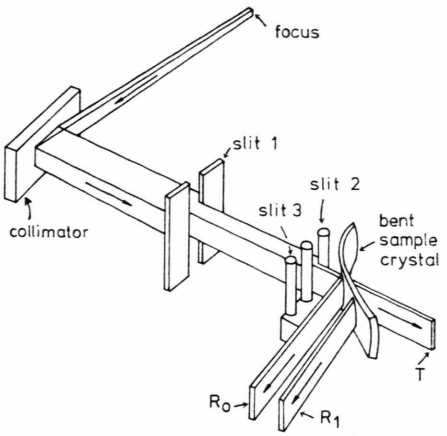

Fig. 1. Experimental set up.

Information about the beam propagation within the deformed crystal is obtained by measuring the intensity profiles of beams R_0, R_1, and T and the separation d between beams R_0 and R_1 as functions of the sample's orientation with respect to the collimating crystal and as functions of the deformation state of the sample. The separation d and the intensity of R_1 is then compared with theoretical values calculated from the Bragg case beam propagation theory the principles of which are briefly outlined in section 3. Results for wavefields of either type, i. e. with anomalous low and with anomalous high absorption, are given below.

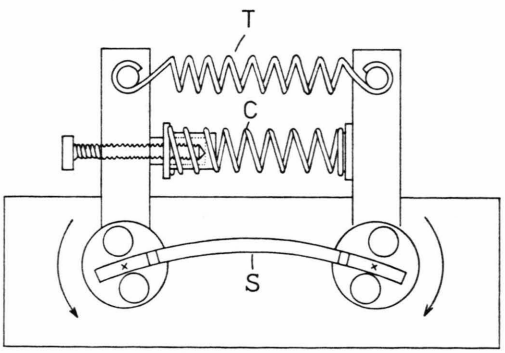

Fig. 2. Scheme of the bending jig showing tension spring T and adjustable compression spring C. S sample crystal.

Considerable care is taken to insure uniformity of the deformation by employing a special four point bending jig shown in Figs. 2 and 3. By using a tension spring T combined with a compression spring C it is possible to achieve positive and negative curvature of the 444 Bragg planes. The sections of the sample which are in contact with the four bending posts are decoupled from the rest of the sample by cuts as shown in Fig. 4 in order to keep away nonuniform strain generated at the contact points from the crystal section through which the X-rays propagate. Also the cuts allow the sample to bend freely about an axis normal to the main bending axis thus complying to the forces of cross tension (compression) arising on either side of the neutral plane of the sample. This kind of bending is referred to as *secondary bending* in the following. Since the axis of the secondary bending lies in the plane of the wave vectors $\boldsymbol{K}_0$ and $\boldsymbol{K}_h$ of the plane wave components it has no first order effect on the wavefield propagation.

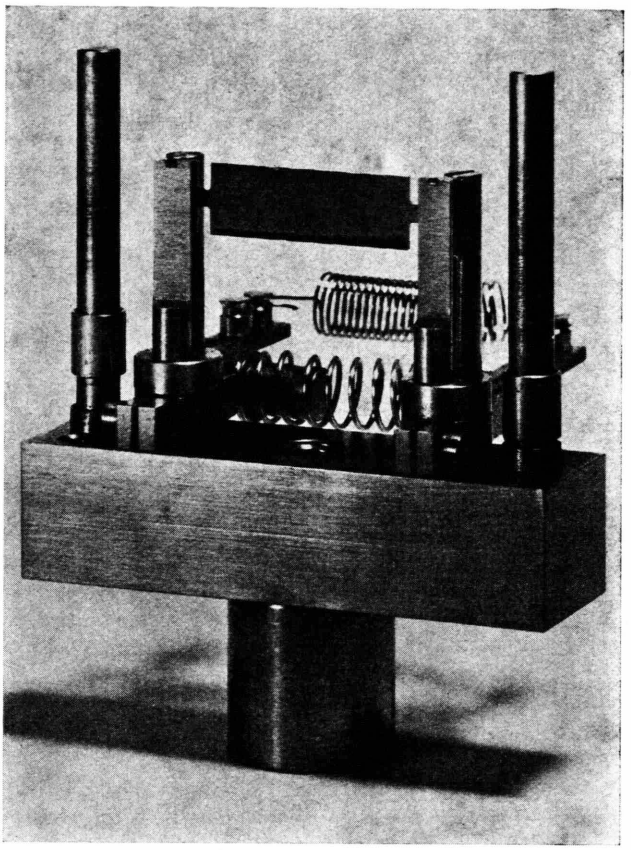

Fig. 3. Bending jig with sample crystal, but slits 2 and 3 removed. The base is 50 mm long.

The radius of curvature is measured with the help of a second ribbon beam which can be made incident on the sample through slit 3 when slit 1 is removed (Fig. 1). On rocking the sample two rocking curves with an angular separation φ are measured. The radius of curvature R is then calculated from $R = \Delta x/\varphi \sin\Theta$ where Δx is the separation of the two ribbon beams and Θ the Bragg angle.

In the beam tracking experiment the width of the incident ribbon beam is set to about 80 microns resulting in an additional beam divergence due to slit diffraction of 0.18 sec of arc, thus matching just

the intrinsic divergence of the asymmetric reflection of 0.17 sec of arc. The slit width is limiting the precision to which the beam separation d can be measured. On the other hand the beam divergence is limiting the definition of the amplitude ratio $\xi \equiv D_h/D_0$ of the wavefield beam and therefore the definition of its initial direction. A slit width of 80 microns with 0.18 sec of arc divergence was found to be a reasonable compromise between exact knowledge of the source location of the wavefield beam and no definition of its initial direction on one hand and poor definition of the source location of the wavefield beam and exact definition of its initial propagation direction on the other.

The employment of molybdenum radiation with silicon crystals allows the tracking of deviated beams over paths up to one or two mm long thereby increasing the accuracy considerably compared to an earlier experiment of similar aspect where due to the use of copper radiation with germanium crystals the length of observable beam paths was absorption limited to about 250 microns.

The sample was cut from dislocation free silicon to a size 30 mm wide, 7 mm high, and 0.75 mm thick. Both sides were lapped with diamond lapping paste to optical smoothness. After lapping the sample was etched for 15 min in a solution consisting of 1 volume part HF 40% and 19 volume parts HNO_3 60%. The etch reduced the thickness to finally 0.64 mm. The crystallographic orientation of the sample is indicated in Figure 4.

3. Theory

In the following a brief summary of the Bragg case beam propagation theory is given. For further details see the earlier publication [1a]. The state of the wavefield is characterized by the so called wavefield vector $\boldsymbol{w} \equiv \boldsymbol{K}_0 + \boldsymbol{K}_h$ and the amplitude ratio $\xi \equiv D_h/D_0$, where $\boldsymbol{K}_0$, $\boldsymbol{K}_h$ are the wave vectors and D_h, D_0 the amplitudes of the plane waves 0 and H of the wavefield. Then, with $k \equiv \lambda_v^{-1}$, λ_v vacuum wavelength, C polarization factor, χ_0, χ_h, $\chi_{\bar{h}}$ the Fourier coefficients of order 0, h, $-h$ of the complex dielectric susceptibility χ, the fundamental equations become

$$(\boldsymbol{w}-\boldsymbol{h})^2 - 4k^2(1+\chi_0+\chi_{\bar{h}} C\,\xi) = 0\,,$$
$$(\boldsymbol{w}+\boldsymbol{h})^2 - 4k^2(1+\chi_0+\chi_h C\,\xi^{-1}) = 0\,.$$

$\boldsymbol{w} = \boldsymbol{w}_r + \mathrm{i}\,\boldsymbol{w}_i$ has the real part $\boldsymbol{w}_r$ and the imaginary part $\boldsymbol{w}_i$. With $\boldsymbol{f} \equiv \boldsymbol{w}_r/|\boldsymbol{w}_r|$ and $\boldsymbol{n} = \boldsymbol{h}/|\boldsymbol{h}|$ as unit vectors of the $\boldsymbol{f}$, $\boldsymbol{n}$ orthogonal system the unit vector $\boldsymbol{j}$ of the direction of energy flow takes the form

$$\boldsymbol{j} = B_1^{-1}[(1+|\xi|^2)\cos\Theta\,\boldsymbol{f} - (1-|\xi|^2)\sin\Theta\,\boldsymbol{n}]$$

where $\quad B_1 \equiv [1+|\xi|^4+2|\xi|^2\cos 2\Theta]^{1/2}$.

Note that $\boldsymbol{j}$ is fully determined by the parameter ξ of the wavefield.

The coefficient of absorption σ_j for propagation in the direction $\boldsymbol{j}$ can be expressed in terms of ξ as

$$\sigma_j = \sigma_0 B_1^{-1}(1+|\xi|^2 + 2C\,\xi_r\,\chi_{ih}/\chi_{i0})$$

where $\sigma_0 \equiv -2\pi k\,\chi_{i0}$ is the normal absorption coefficient and χ_{i0}, χ_{ih} are the Fourier coefficients of order 0 and h of the imaginary part χ_i of the dielectric susceptibility $\chi = \chi_r + \mathrm{i}\,\chi_i$.

The path of a wavefield beam of a given initial state ξ is calculated by advancing in steps of length $\mathrm{d}l$ along the local propagation direction $\boldsymbol{j}$. We consider the wavefield beam of state ξ_0 at $\boldsymbol{r}_0$. It propagates to $\boldsymbol{r} = \boldsymbol{r}_0 + \boldsymbol{j}_0\,\mathrm{d}l$. Small lattice distortions can be described as locally varying reciprocal lattice vectors $\boldsymbol{h}(\boldsymbol{r})$, and proceeding from $\boldsymbol{r}_0$ by $\delta\boldsymbol{r}$ the lattice has changed by $\delta\boldsymbol{h} = \nabla\boldsymbol{h}\cdot\delta\boldsymbol{r}$. Similarly the local variations $\delta\boldsymbol{w}$ of $\boldsymbol{w}$ which are necessary to keep the propagating wavefield fitted to the varying lattice are assumed to be small and expressible with a continuous function $\boldsymbol{w}(\boldsymbol{r})$ as $\delta\boldsymbol{w} = \nabla\boldsymbol{w}\cdot\delta\boldsymbol{r}$.

The obvious postulate that the wavefield is to obey the fundamental equations also in the new location $\boldsymbol{r}_0 + \boldsymbol{j}_0\,\mathrm{d}l$ is by no means sufficient to define uniquely the changes $\mathrm{d}\boldsymbol{h}$ and $\mathrm{d}\xi$ of the wavefield suffered when propagating by $\boldsymbol{j}_0\,\mathrm{d}l$. We therefore make additional assumptions about the interaction of the wavefield with the slightly distorted lattice, namely

(a) the fundamental equations must be fulfilled not only at $\boldsymbol{r}_0$ and at $\boldsymbol{r}_0 + \boldsymbol{j}_0\,\mathrm{d}l$ but at any position $\boldsymbol{r}_0 + \delta\boldsymbol{r}$ with an *arbitrary* infinitesimal $\delta\boldsymbol{r}$,

(b) $\boldsymbol{w}(\boldsymbol{r})$ must maintain its ray properties, i. e. $\nabla\times\boldsymbol{w} = 0$ at any position $\boldsymbol{r}_0 + \delta\boldsymbol{r}$.

(c) the variations of $\boldsymbol{w}(\boldsymbol{r})$ must be smallest, i. e $I \equiv \nabla\boldsymbol{w}\ ..\ \nabla\boldsymbol{w}^*$ shall be minimal. (I is the so called double scalar product of the tensor $\nabla\boldsymbol{w}$. Given for instance an orthogonal coordinate system $\boldsymbol{f}$, $\boldsymbol{n}$, $\boldsymbol{e}$, I is the sum of the squares of the partial derivatives of $\boldsymbol{w}_r$ and $\boldsymbol{w}_i$ with respect to the coordinates.)

The correctness of the assumptions (a) to (c) or even their plausibility has been questioned and argued in the past. The very good agreement of the ray tracking experiments reported in this paper with

the above theory is strongly supporting these assumptions. Furthermore, it is interesting to note that the treatment given by PENNING and POLDER [7] is comprised in this theory as the limiting case where $\boldsymbol{w}$ and ξ take only real values. Another interesting result is that mere fanning of the Bragg planes should influence the wavefield beam provided the imaginary part of ξ is big enough.

Employing some vector analysis we obtain the searched-for variations $\mathrm{d}\boldsymbol{w}$ and $\mathrm{d}\xi$:

$$\mathrm{d}\boldsymbol{w} = \boldsymbol{j}\cdot\nabla\boldsymbol{w}\,\mathrm{d}l\,,\mathrm{d}\boldsymbol{h} = \boldsymbol{j}\cdot\nabla\boldsymbol{h}\,\mathrm{d}l$$

$$\nabla\boldsymbol{w} = |\boldsymbol{p}_0|^{-2}(-|\boldsymbol{p}_0|^{-2}\boldsymbol{p}_0\cdot\nabla\boldsymbol{h}\cdot\boldsymbol{q}_0\,\boldsymbol{p}_0{}^*\,\boldsymbol{p}_0{}^* + \nabla\boldsymbol{h}\cdot\boldsymbol{q}_0\,\boldsymbol{p}_0{}^* + \boldsymbol{p}_0{}^*\nabla\boldsymbol{h}\cdot\boldsymbol{q}_0)$$

$$\mathrm{d}\xi = -k^{-2}C^{-1}\chi_h{}^{-1}\cdot(1-\xi_0{}^2)^{-1}\xi_0{}^2(\boldsymbol{w}_0\cdot\mathrm{d}\boldsymbol{w} + \boldsymbol{h}_0\cdot\mathrm{d}\boldsymbol{h}).$$

With small deformations the tensor $\nabla\boldsymbol{h}$ can be expressed in terms of the curvature FF, the fanning FN, and the gradient of the distance of the Bragg planes NN directly:

$$\nabla\boldsymbol{h} = -2k\sin\Theta\cdot[FF\,\boldsymbol{f}\boldsymbol{f} + FN(\boldsymbol{n}\boldsymbol{f}+\boldsymbol{f}\boldsymbol{n}) + NN\,\boldsymbol{n}\boldsymbol{n}]$$

where $\boldsymbol{s}\boldsymbol{f}$, $\boldsymbol{f}\boldsymbol{u}$, $\boldsymbol{n}\boldsymbol{f}$, and $\boldsymbol{n}\boldsymbol{u}$ are dyadic products. FF, FN, and NN are to be calculated from the second derivatives $\nabla\nabla(\boldsymbol{u}\cdot\boldsymbol{n})$ of $\boldsymbol{u}\cdot\boldsymbol{n}$, the component normal to the Bragg planes of the displacement vector $\boldsymbol{u}$:

$$FF = \boldsymbol{f}\cdot(\boldsymbol{f}\cdot\nabla\nabla(\boldsymbol{u}\cdot\boldsymbol{n}))\,,$$
$$FN = \boldsymbol{f}\cdot(\boldsymbol{n}\cdot\nabla\nabla(\boldsymbol{u}\cdot\boldsymbol{n}))\,,$$
$$NN = \boldsymbol{n}\cdot(\boldsymbol{n}\cdot\nabla\nabla(\boldsymbol{u}\cdot\boldsymbol{n}))\,.$$

It is $FF = R^{-1}$, where R is the radius of curvature of the Bragg planes. With FF, FN, and NN we obtain

$$\mathrm{d}\xi = 4\sin\Theta\,\xi_0(C\,\chi_h B_1 B_2{}^2)^{-1}(A_{ff}\cos^2\Theta\,FF + A_{nn}\sin^2\Theta\,NN + A_{fn}\sin\Theta\cos\Theta\,FN)\,\mathrm{d}l$$

where

$$A_{ff} = \xi_0[a_1{}^*(T_1+2T_2)\,G_1 + a_2{}^*T_2\,G_2],$$
$$A_{nn} = -\xi_0[a_2{}^*(2T_1+T_2)\,G_2 + a_1{}^*T_1\,G_1],$$
$$A_{fn} = \xi_0(G_2\,a_1 - G_1\,a_2)\,(a_2{}^{*2}\tan\Theta + a_1{}^{*2}\cot\Theta),$$
$$T_1 = (1+|\xi_0|^4 + 2\,\mathrm{Re}(\xi_0{}^2))\cos^2\Theta\,,$$
$$T_2 = (1+|\xi_0|^4 - 2\,\mathrm{Re}(\xi_0{}^2))\sin^2\Theta\,,$$
$$B_2 = T_1+T_2 = 1+|\xi_0|^4 + +2\,\mathrm{Re}(\xi_0{}^2)\cos 2\Theta\,,$$
$$a_1 = (\xi_0{}^2+1)\cos\Theta\,,$$
$$a_2 = (\xi_0{}^2-1)\sin\Theta\,,$$
$$G_1 = (|\xi_0|^2+1)\cos\Theta\,,$$
$$G_2 = (|\xi_0|^2-1)\sin\Theta\,.$$

4. Deformation State of the Sample

We choose a coordinate system as shown in Fig. 4 with unit vectors

$$x_1 \equiv \boldsymbol{e} = [\bar{1}\bar{1}2]/\sqrt{6}\,,$$
$$x_2 \equiv \boldsymbol{n} = [111]/\sqrt{3}\,,$$
$$x_3 \equiv \boldsymbol{f} = [1\bar{1}0]/\sqrt{2}\,.$$

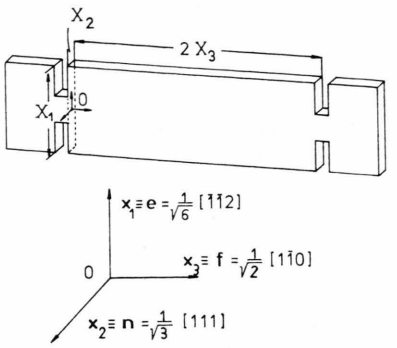

Fig. 4. Shape of the sample crystal and cristallographic orientation.

The sample is bent by moments M exerted by the bending posts through the reduced cross section at the cuts (Figure 4). According to MILNE-THOMSON [10] the displacement vector $\boldsymbol{u}$ is given by

$$u_1 = M/2\,I\,(2\,S_{13}\,x_1\,x_2 + S_{36}\,x_2{}^2 + S_{35}\,x_2(x_3 - X_3))$$
$$u_2 = M/2\,I\,(-S_{13}\,x_1{}^2 + S_{23}\,x_2{}^2 + S_{33}(x_3 - X_3)^2 - S_{35}\,x_1(x_3 - X_3))$$
$$u_3 = M/2\,I\,(S_{35}\,x_1\,x_2 + S_{34}\,x_2{}^2 + 2\,S_{33}\,x_2(x_3 - X_3))$$

where $I = X_1\,X_2{}^3/12$. $2\,X_3$ is the length, X_1 is the height and X_2 is the thickness of the sample. S_{ik} are the inverse elastic moduli with respect to the system $\boldsymbol{e}$, $\boldsymbol{n}$, $\boldsymbol{f}$. Values for the inverse moduli with respect to the cubic axes are:

$$S_{11}{}^0 = 7.74\cdot10^{-13}\,\mathrm{cm}^2\,\mathrm{dyn}^{-1}\,.$$
$$S_{12}{}^0 = -2.17\cdot10^{-13}\,\mathrm{cm}^2\,\mathrm{dyn}^{-1}\,,$$
$$S_{44}{}^0 = 12.60\cdot10^{-13}\,\mathrm{cm}^2\,\mathrm{dyn}^{-1}\,.$$

Transforming the inverse moduli in the $\boldsymbol{e}$, $\boldsymbol{n}$, $\boldsymbol{f}$ system we obtain

$$S_{13} = -1.57\cdot10^{-13}\,\mathrm{cm}^2\,\mathrm{dyn}^{-1}\,,$$
$$S_{23} = -0.97\cdot10^{-13}\,\mathrm{cm}^2\,\mathrm{dyn}^{-1}\,,$$
$$S_{33} = 5.93\cdot10^{-13}\,\mathrm{cm}^2\,\mathrm{dyn}^{-1}\,,$$
$$S_{36} = 1.70\cdot10^{-13}\,\mathrm{cm}^2\,\mathrm{dyn}^{-1}\,,$$
$$S_{34} = S_{35} = 0\,.$$

With these values we calculate for the 444 Bragg planes

$$FF = -S_{33}\,M/I = R^{-1}\,,\ FN = 0\,,$$
$$NN = S_{23}\,M/I = 0.164\,R^{-1}\,.$$

We note, that the deformations FF, FN, NN are constant throughout the sample volume traversed by X-rays in the experiment. Consequently the calculation of ray paths and intensities is considerably simplified. Also, $FN=0$ and $|NN|<|FF|$ which implies that the ray deflection is mainly caused by the curvature of the Bragg planes and to a lesser extent by the gradient of the distance of the planes. The predominance of the influence of FF over that of NN is enhanced by the fact that in the calculation of $d\xi$ FF is weighed by $\cos^2\Theta$ and NN by $\sin^2\Theta$ and that $\sin^2\Theta/\cos^2\Theta \ll 1$ for the silicon 444 reflection of MoKα radiation.

In the experiment the radius of curvature was varied approximately between $R=30$ m and $R=110$ m.

5. Results

Experimentell evidence for the occurrence of a beam R_1 (Fig. 1) as the outside continuation of the internally bent back Bragg case wavefield beam is given in Figs. 5, 7, and 8.

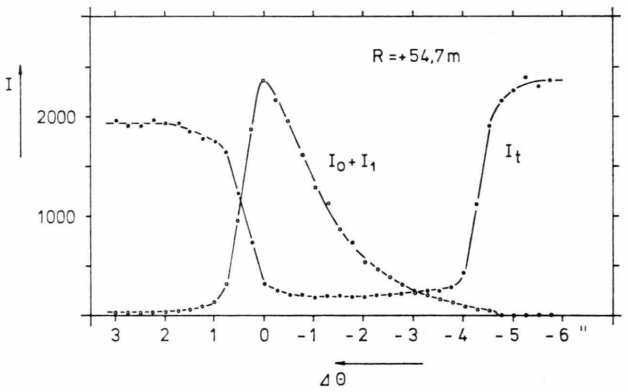

Fig. 5. Plot of intensity I_0+I_1 of the Bragg reflected beam R_0 and the bent back beam R_1 and intensity I_t of the transmitted beam T versus the rocking angle $\Delta\Theta$.

In Fig. 5 the sum I_0+I_1 of the intensities I_0 of beam R_0 and I_1 of beam R_1 is plotted together with the intensity I_t of the transmitted beam T while the sample (bent to $R=54.7$ m) is rocked with respect to the fore crystal over a range of about 7 sec of arc. As is well known from the perfect crystal dynamical theory when rocking the second crystal in a nondispersive double crystal arrangement with symmetrical reflection the parameter.

$$y=|C|^{-1}|\chi_{rh}|^{-1}(|\chi_{r0}|-\sin 2\Theta\,\Delta\Theta)$$

is varied denoting the point in the reflection range, where $\Delta\Theta=\Theta-\Theta_B$ is the deviation from the geometrical Bragg angle. To get the same value for each polarization state for a given $\Delta\Theta$ we define $y_c=y|C|\cdot y=0$ corresponds to the center and $y=\pm 1$ to the limits of the range of maximum reflection (which in the special case of total absence of absorption is strictly total). With the scanning of y the entering direction of the wavefield beam sweeps from the direction of the incident wave to an orientation nearly parallel to the surface and back to its original direction. Note that I_t remains at a low level of about 10% not only for $|y|\leqq 1$ where the conventional Bragg peak in I_0 with a width not exceeding about 1 sec of arc occurs. I_t is small over a much wider range extending on the low Bragg angle wing of the Bragg peak as far as 4 sec of arc. It is in this range where the Bragg case wavefield is travelling back to the entrance surface.

In Fig. 5 the position of the Bragg peak I_0 is at about 0 sec of arc. Here $I_1\approx 0$. To the right I_0 falls rapidly to zero while I_1 first increases and finally decreases to zero too. At the same angle I_t attains its original value. Here the path of the entering wavefield is so little curved that it reaches the rear surface of the sample before the beam is pointing back towards the entrance surface. In order to illustrate this behaviour a set of beam paths with different entering directions was calculated for a fixed radius R of curvature of the sample (Figure 6). Note that with a given sign of R wavefields belonging to only one side of the Bragg peak can be curved back to the surface. If $R>0$ ($R<0$) wavefields of anomalous low (high) absorption are

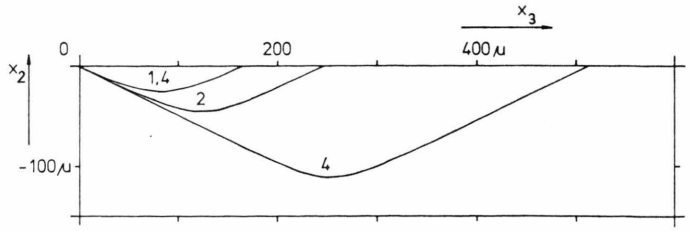

Fig. 6. Set of calculated beam paths for fixed R and varying y_c (values given at each path).

affected by the curvature of the lattice planes. Correspondingly $I_0 + I_1$ is asymmetric and the Bragg peak I_0 lies at the (left) edge of the range of low I_t in Figure 5.

Fig. 7 is a photograph of beams R_0 and R_1 demonstrating their simultaneous existance and distinct spacial separation. It was taken with a fixed orienta-

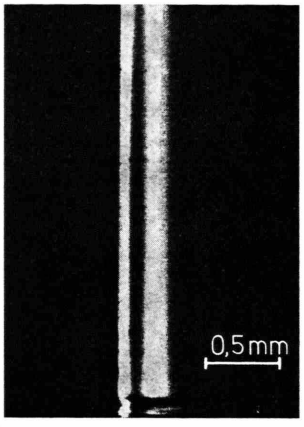

Fig. 7. Photo of beams R_0 (left) and R_1 (right).

tion of the sample and $R = 109.4$ m. The variation of the distance d between beams R_0 and R_1 with y_c and the entering direction of the wavefield beam is illustrated by Figure 8. Here R_0 and R_1 have been photographed when the sample was not properly

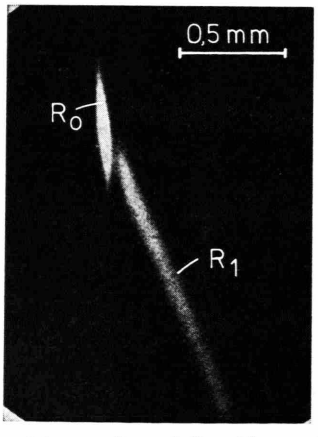

Fig. 8. Photo of beams R_0 and R_1 with sample misaligned about a horizontal axis.

aligned about the axis parallel to **f** in Figure 4. Regarding the incident ribbon beam such misalignment results in a linear variation of y_c from top to bottom in the beam. Consequently wavefields with different y_c are excited simultaneously and at vertically separated locations and can thus be recorded on just one picture. The center of the Bragg peak ($y_c = 0$) lies near a point at half height in the image of R_0. Below (above) this point wavefields of low (high) absorption are excited. Clearly in Fig. 8 only wavefields of low absorption curve back to the entrance surface. This is in accordance with the fact that R was positive when Fig. 8 was taken. Also, the increase of d with increasing y_c is evident from Figure 8.

The quantitative dependence of d on y_c is illustrated in Figure 9. The points have been obtained by densitometric evaluation of photos similar to that shown in Figure 8. The curve has been calculated from the theory above. Except for values of y_c close to 1 the agreement is very good.

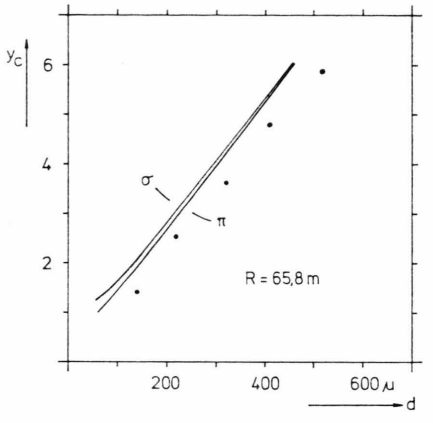

Fig. 9. Comparison of measured (points) and calculated (curves) dependence of d on y_c for polarization states σ and π.

In Fig. 10 measured intensities I_1 divided by the intensity I_i of the incident beam (points) are plotted over d together with theoretical intensities (curves) for $R = 65.8$ m and $R = -63.3$ m. Note that $R < 0$ implies that R_1 is formed by wavefields with high absorption. Again the agreement is very good. Beam separations up to 0.6 mm contribute to the comparison.

All curves were calculated with a value of 0.819 for χ_{ih}/χ_{i0} which was taken from calculations by HILDEBRANDT [11]. An even better fit is achieved if 0.59 is used in the path calculations, as may be seen from the broken curves in Figure 10. This may be evidence that the correct value for χ_{ih}/χ_{i0} is smaller than that given by HILDEBRANDT. To investigate this point further an independent measurement of χ_{ih}/χ_{i0} for the silicon 444 reflection of MoKα-radiation is necessary.

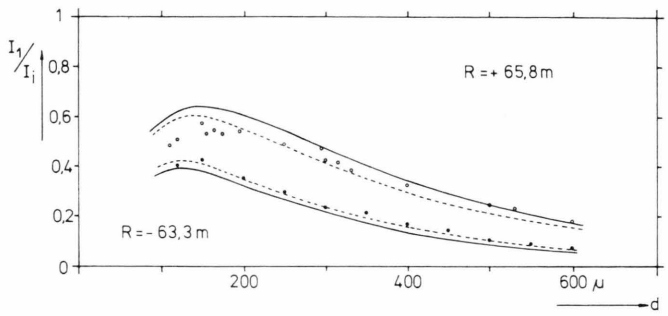

Fig. 10. Plot of intensity I_1 versus beam separation d, points experimental, curves calculated. Upper values with $R>0$ and low absorption, lower ones with $R<0$ and high absorption. The broken curves have been calculated with a modified value $\chi_{ih}/\chi_{i0}=0.59$.

An equally good agreement as that shown in Fig. 10 was observed with $I_1(d)$ measurements with $R=+33.1$ m, $+109.4$ m, -32.0 m.

The experimental evidence confirming the Bragg case beam theory of Sect. 3 is therefore broadly founded and thus quite convincing. As a next step it would be very interesting to check the somewhat surprising prediction of the theory that the fanning FN of Bragg planes influences a wavefield provided its imaginary part ξ_i of ξ is large enough.

[1a] U. Bonse, Z. Physik **177**, 385 [1964].
[1] P. P. Ewald, Ann. Physik **54**, 519 [1917]; Z. Physik **2**, 332 [1920]; Z. Physik **30**, 1 [1924]; Phys. Z. **26**, 29 [1925].
[2] M. v. Laue, Ergebn. exakt. Naturwiss. **10**, 133 [1931].
[3] U. Bonse, Z. Physik **177**, 529 [1964].
[3a] G. Hildebrandt, Z. Kristall. **112**, 340 [1959].
[4] J. Scharschmidt, H. Klapper, and H. Arenhövel, Z. Physik **180**, 317 [1964].
[5] E. S. Meieran and I. A. Blech, J. Appl. Phys. **43**, No. 2, 265 [1972].
[6] E. J. Saccocio, Appl. Phys. Letters **17**, 149 [1970].
[7] P. Penning and D. Polder, Philips Res. Repts. **16**, 419 [1961].
[8] N. Kato, J. Phys. Soc. Japan **18**, 1785 [1963]; J. Phys. Soc. Japan **19**, 67 [1964]; J. Phys. Soc. Japan **19**, 971 [1964].
[9] K. Kambe, Z. Naturforsch. **20 a**, 770 [1965; Z. Naturforsch. **23 a**, 25 [1968].
[10] L. M. Milne-Thomson, Antiplane Elastic Systems, Springer Verlag, Berlin 1962, p. 204.
[11] G. Hildebrandt, private communication.